RSC Advances

PAPER

View Article Online
View Journal | View Issue

Cite this: *RSC Adv.*, 2025, **15**, 49933

Hydrogenation-enriched fundamental properties of armchair silicene nanoribbons: a comprehensive first-principles study

D. M. Hoat,[ab] Duong Trong Nhan,[d] Vuong Minh Duc,[e] Le Phuong Truong,[f] Tam V.-T. Mai,[gh] Minh Triet Dang[i] and Duy Khanh Nguyen *[cd]

In this study, density functional theory (DFT) calculations are systematically performed to explore structural, electronic, and magnetic properties of hydrogen-adsorbed 7-armchair silicene nanoribbons (7ASiNRs) with diverse hydrogenations, revealing unexpected physical behaviors. All optimized configurations exhibit good structural stability, whereas hydrogen atoms preferentially occupy top sites of Si atoms and double-side adsorption is energetically favored. Interestingly, although most even-hydrogenated configurations behave as nonmagnetic semiconductors with direct bandgaps, the $(2H)_{1-14}$ and $(2H)_{4-11}$ configurations exhibit anomalous magnetic moments, raising attention about the dependence of magnetism on the distance between adsorbed atoms. Moreover, the $(7H)_{single}$ configuration shows a remarkably large magnetization of 7 μ_B, originating from unpaired Si-$3p_z$ electrons localized on the unpassivated side. To clarify these phenomena, systematic analyses of orbital-, atom-, and spin-decomposed band structures, DOSs, charge, and spin density distributions are performed, demonstrating that the hybridization between H-1s and Si-(3s, $3p_{xy}$, $3p_z$) orbitals govern the structural reconstructions, charge redistribution, and spin polarization. These findings uncover new mechanisms of magnetism and bandgap modulation in hydrogen-adsorbed 7ASiNRs, highlighting the essential role of hydrogen adsorption in tuning electronic and magnetic properties. The results provide valuable guidance for designing 2D silicon-based materials with controllable magnetic and electronic characteristics for future nanoelectronic and spintronic device applications.

Received 11th November 2025
Accepted 8th December 2025

DOI: 10.1039/d5ra08700g

rsc.li/rsc-advances

1. Introduction

Two-dimensional (2D) materials have been a central focus of condensed matter and materials science owing to their remarkable structural versatility and tunable physicochemical properties. Since the isolation of graphene, a broad class of 2D systems, including silicene, germanene, phosphorene, transition metal dichalcogenides (TMDs), germanium sulfide, gallium selenide, and Janus MoSSe has been either synthesized or theoretically predicted, exhibiting diverse electronic behaviors such as semimetallicity, semiconductivity, and topologically nontrivial states.[1–10] Their reduced dimensionality enables exceptional carrier mobility, strong spin–orbit coupling, and quantum confinement effects, which collectively underpin novel phenomena such as the quantum spin Hall effect, valley polarization, and high-efficiency charge transport. These advances highlight the vast potential of 2D materials as the foundation for next-generation nanoelectronic and spintronic technologies.

Beyond the 2D regime, dimensional reduction to one-dimensional (1D) nanostructures offers additional routes for electronic structure engineering. Confining a 2D layer into a nanoribbon geometry introduces edge effects, localized states, and subband quantization, all of which strongly influence the material's fundamental characteristics.[11–18] Among 2D analogues, silicene, a low-buckled honeycomb allotrope of silicon, has attracted substantial interest as a graphene-like material compatible with existing silicon-based platforms.[19–21] When designed into nanoribbons, silicene exhibits pronounced width- and edge-dependent properties, with armchair and zigzag configurations displaying distinct electronic and

[a]*Institute of Theoretical and Applied Research, Duy Tan University, Hanoi 100000, Vietnam*
[b]*School of Engineering and Technology, Duy Tan University, Da Nang 550000, Vietnam*
[c]*Laboratory for Computational Physics, Institute for Computational Science and Artificial Intelligence, Van Lang University, Ho Chi Minh City, Vietnam. E-mail: khanh.nguyenduy@vlu.edu.vn*
[d]*Faculty of Mechanical, Electrical, and Computer Engineering, Van Lang School of Technology, Van Lang University, Ho Chi Minh City, Vietnam*
[e]*VNU-HCM High School for the Gifted, Ho Chi Minh City, Vietnam*
[f]*Faculty of Mechatronics and Electronics, Lac Hong University, No. 10 Huynh Van Nghe Str, Tran Bien Ward, Dong Nai Province, Vietnam*
[g]*Faculty of Chemistry, University of Science, 227 Nguyen Van Cu, Cho Quan Ward, Ho Chi Minh City, Vietnam*
[h]*Vietnam National University, Vo Truong Toan Street, Quarter 33, Linh Xuan Ward, Ho Chi Minh City, Vietnam*
[i]*School of Education, Can Tho University, Can Tho City, Vietnam*

magnetic behaviors.[22,23] This structural tunability renders silicene nanoribbons (SiNRs) ideal model systems for exploring low-dimensional phenomena and for the development of Si-compatible nanoscale devices.

Silicene nanoribbons have been realized experimentally *via* epitaxial growth on metallic substrates such as Ag(110) and ZrB_2(0001), as well as through top-down nanofabrication methods.[24,25] These ribbons exhibit semiconducting, metallic, or magnetic ground states depending on their edge geometry, width, and surface passivation. In particular, armchair silicene nanoribbons (ASiNRs) exhibit direct and tunable bandgaps, mechanical stability, and high carrier mobility, making them attractive candidates for field-effect transistors, chemical sensors, thermoelectric converters, and spintronic elements.[26–28] Theoretical investigations have further shown that the electronic properties of ASiNRs can be effectively controlled by width modulation, edge reconstruction, external fields, or chemical functionalization, providing a versatile means of tailoring their quantum and transport characteristics.

Despite these promising attributes, the intrinsic semiconducting and nonmagnetic nature of pristine ASiNRs limits their functional diversity. Several approaches have been proposed to tune their electronic and magnetic properties, including application of external electric fields, substitutional doping, and surface adsorption.[29–32] It is worth noting that external electric fields may cause some practical limits in 1D materials. In zigzag graphene nanoribbons, for example, external transverse electric fields have been shown to drive a transition to a half-metallic state, enabling spin-polarized transport that is tunable by field strength.[33] However, the electric fields required to realize such effects are often quite large and challenging to achieve experimentally. As an alternative, noninvasive optical and mechanical stimuli have been demonstrated to reversibly modulate spin polarization through dipole-induced symmetry breaking at the nanoribbon edges, eliminating the need for high electric fields.[34] Among these strategies, hydrogenation is particularly appealing due to its experimental feasibility and strong impact on orbital hybridization and local electronic structure. Hydrogen adsorption can convert Si–Si bonding from sp^2 to sp^3 configurations, modify bandgaps, and induce magnetic moments without introducing significant lattice distortion. However, most existing studies have focused on uniform or symmetric hydrogen adsorption in silicene,[35–38] leaving the effects of diverse hydrogen coverages and distributions largely unexplored in silicene nanoribbons. In this study, a comprehensive investigation of hydrogenated armchair silicene nanoribbons (7ASiNRs) under various adsorption patterns is therefore essential to uncover new structure–property relationships, elucidate the underlying mechanisms of electronic and magnetic modulation, and enable rational design of silicene-nanoribbon-based materials for advanced nanoelectronic and spintronic applications.

2. Computational method

In computational materials design, Vienna *ab initio* simulation package (VASP) based on the density functional theory framework has been effectively utilized to explore material properties.[35,39–44] In this study, using VASP calculations, the structural, electronic, and magnetic characteristics of pristine and hydrogen-adsorbed 7ASiNRs were fully revealed. The armchair silicene nanoribbon structures were constructed by cutting a monolayer silicene sheet along the armchair y direction to form one-dimensional periodic unit cells, while maintaining a vacuum spacing of 15 Å along the z-axis to eliminate spurious interactions between neighboring images. The edge Si atoms were terminated with hydrogen to remove dangling bonds and stabilize the ribbon edges.

The exchange–correlation potential was described using the generalized gradient approximation (GGA) with the Perdew–Burke–Ernzerhof (PBE) functional.[45] The interactions between valence electrons and ionic cores were represented by projector augmented-wave (PAW) pseudopotentials.[46] A kinetic energy cutoff of 500 eV was applied for the plane-wave basis. The atomic positions were fully relaxed until the total energy and atomic forces were converged within the thresholds of 10^{-7} eV and 10^{-2} eV $Å^{-1}$, respectively. For Brillouin zone sampling, a Monkhorst–Pack k-point grid of $12 \times 1 \times 1$ was used for structure optimization, followed by a denser $100 \times 1 \times 1$ grid for self-consistent electronic and magnetic calculations. Spin polarization was incorporated by setting the proper ISPIN and MAGMOM parameters in VASP to explore possible magnetic ground states. Based on the optimized geometries, the 1D electronic band structures were subsequently calculated along the Γ–K path in reciprocal space of the 1D Brillouin zone.

3. Result and discussion

In this study, the one-dimensional strips of silicene monolayer were constructed by cutting across the buckled hexagonal lattice along the armchair direction. In the 7ASiNR, there are seven parallel Si–Si dimer rows bridging the two opposite armchair edges. As shown in Fig. 1(a), the optimized pristine 7ASiNR inherits the intrinsic buckled structure of silicene,[47] where the two sublattices of the honeycomb are slightly displaced out of plane, so that half the Si atoms lie in an "upper" plane and the other half in a "lower" plane. This buckled honeycomb arrangement originates from the mixed sp^2/sp^3 hybridization characteristic of silicence.[48,49] The 7ASiNR with unsaturated edges is highly reactive and will undergo significant reconstruction to lower its energy.[50] To prevent these effects, the edge Si atoms are passivated with hydrogen atoms, where each edge Si atom binds to one H atom to maintain an sp^2-like planar edge bonding.

Hydrogen adsorption can strongly influence both the structural and electronic properties of nanoribbons.[13,16] The effects vary depending on the concentration and spatial distribution of the adatoms. To establish a relationship between these factors, the 7ASiNRs with all possible hydrogen adsorption were modeled and optimized. To evaluate the structural stability of configurations, the adsorption energies (E_{ads}) of all configurations were carefully calculated. As a result, 17 stable configurations with significant negative E_{ads} were found and presented in Table 1, in which each of these configurations is labeled with

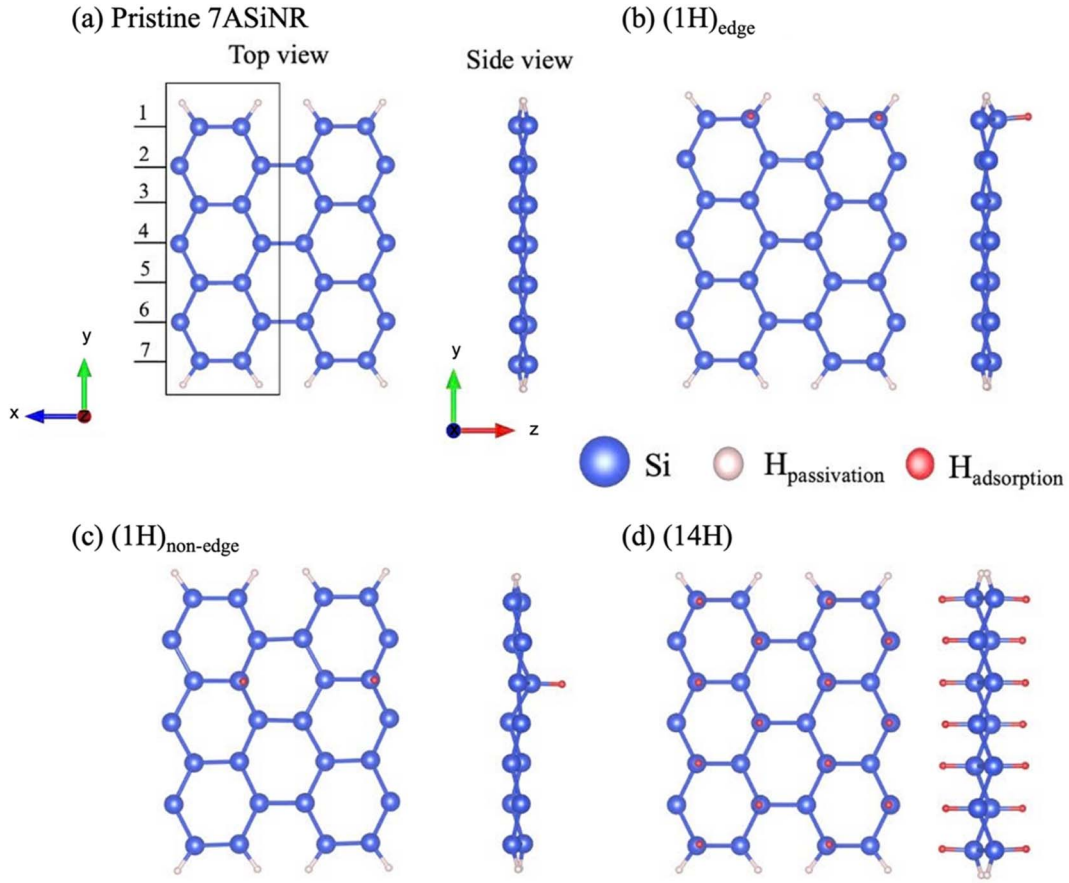

Fig. 1 Optimized structures of (a) pristine 7ASiNR, (b) $(1H)_{edge}$, (c) $(1H)_{non\text{-}edge}$, and (d) (14H) configurations. The solid black number along *y* direction (dimer line) and black rectangle display for the ribbon width and unit cell of the system, respectively.

number of hydrogen adatoms inside parentheses and a subscript that specifies the adsorption site. Specifically, for single adatom adsorption, hydrogen adsorbed at the edge was termed as $(1H)_{edge}$ and hydrogen adsorbed away from the edge was termed as $(1H)_{non\text{-}edge}$; for higher adatom concentrations, such as 7 hydrogen adatoms adsorbed on one side of the nanoribbon was termed as $(7H)_{single}$ and 7 hydrogen adatoms adsorbed on both sides of the nanoribbon was termed as (7H). As shown in Fig. 1(a), the pristine 7ASiNR is characterized by typical hexagonal pattern from the top view and slightly buckling structure from the side view. Hydrogen adsorptions, shown in Fig. 1(b)–(d), mainly increases the local buckling, while the hexagonal structure is preserved. Therefore, the structural changes can be described by considering the bond lengths, in-plane angle, and the buckling. Due to the edge termination, the Si–Si bond lengths vary depending on their positions. In the subsequent analysis, the Si–Si bonds at the edges are denoted as 1st Si–Si, whereas those further from the edges are referred to as 2nd Si–Si. The interaction of H-s orbitals and Si-sp^2/sp^3 orbitals is well reflected through the variation of 1st Si–Si and 2nd Si–Si bond lengths, which are reported in Table 1. For pristine 7ASiNR, the replacement of Si by H atoms at the edge clearly weakens the 1st Si–Si bonds, making them be longer than the 2nd Si–Si bonds, which are 2.28 Å *versus* 2.21 Å, respectively. However, with one more H added to the edge Si atom in the $(1H)_{edge}$ configuration, the interaction between H-s and Si-sp^2/sp^3 become stronger, leading to shorter 1st Si–Si bonds compared to the 2nd Si–Si bonds. It can be deduced that H-s orbitals well hybridize with Si-sp^2/sp^3 strengthening the local Si–Si bonds, meanwhile the nearly Si–Si bonds are weakened due to the transfer of electrons to H-adsorption sites. This relationship is confirmed when considering the $(1H)_{non\text{-}edge}$ and other configurations with more H atoms adsorbed. The distribution of more H atoms throughout the 7ASiNRs, resulting in stronger 2nd Si–Si bonds compared to the 1st Si–Si bonds. Therefore, in (*x*H) ribbons ($x = 2$ to 14), the 2nd Si–Si bonds (2.161–2.340 Å) are always shorter than the 1st Si–Si bonds (2.326–2.351 Å).

It is worth noting that the in-plane angles of free-standing monolayers with sp^2- and sp^3-hybridizations are about 120° and 109.5°, respectively.[51] Meanwhile, the lattices with sp^2/sp^3 hybridization like germanene, stanene and silicene nanoribbons have in-plane angle close to 120°.[52–54] All the H-adsorbed 7ASiNRs, reported in Table 1, have buckling structures, indicating the presence of a portion of sp^3 orbitals. In pristine 7ASiNR, the in-plane angle is 121.48°, which is slightly changed upon the adsorption of small numbers of H atoms. As more than 9H atoms are adsorbed, the contribution of H-s orbitals is large

Table 1 Energy adsorption E_{ads} (eV), maximum Si–Si bond length/1st Si–Si (Å), minimum Si–Si bond length/2nd Si–Si (Å), H–Si bond length (Å), Si–Si–Si angle (°), magnetic moment (μ_B), bandgap (eV), and planar/buckled structure of the pristine and hydrogen-adsorbed 7ASiNR configurations

Configuration	E_{ads} (eV)	1st Si–Si bond length (Å)	2nd Si–Si bond length (Å)	H–Si bond length (Å)	Si–Si–Si angle (°)	Planar/ buckled	Magnetic moment (μ_B)	Bandgap (eV)
Pristine 7ASiNR	✗	2.276	2.205	✗	121.48	Buckled	0	0.65
$(1H)_{edge}$	−2.6155	2.208	2.340	1.502	122.76	Buckled	1.0	Spin up: 0.40, spin dn: 0.25
$(1H)_{non\text{-}edge}$	−2.1955	2.284	2.206	1.507	120.69	Buckled	1.0	Spin up: 0.65, spin dn: 0.24
$(2H)_{1-2}$	−3.0466	2.341	2.210	1.501	121.21	Buckled	0	0.23
$(2H)_{1-6}$	−2.9971	2.351	2.184	1.502	119.76	Buckled	0	0.51
$(2H)_{1-14}$	−2.6493	2.339	2.227	1.502	120.23	Buckled	0.74	Metal
$(2H)_{4-11}$	−2.3001	2.335	2.203	1.506	123.54	Buckled	0.91	Metal
(3H)	−2.8592	2.349	2.208	1.506	119.27	Buckled	1.0	Spin up: 0.55, spin dn: 0.42
(4H)	−2.9474	2.345	2.185	1.502	121.34	Buckled	0	0.33
(5H)	−2.8787	2.349	2.208	1.506	121.67	Buckled	1.0	Spin up: 0.64, spin dn: 0.52
(6H)	−2.9403	2.347	2.205	1.503	120.99	Buckled	0	0.92
$(7H)_{single}$	−2.3194	2.336	2.309	1.515	122.29	Buckled	7.0	Spin up: 1.93, spin dn: 1.00
(7H)	−2.8803	2.349	2.217	1.504	121.02	Buckled	1.0	Spin up: 0.71, spin dn: 0.42
(8H)	−2.9169	2.347	2.195	1.502	122.68	Buckled	0	0.55
(9H)	−2.8773	2.348	2.215	1.504	122.33	Buckled	1.0	Spin up: 0.95, spin dn: 0.67
(10H)	−2.9155	2.346	2.208	1.503	113.82	Buckled	0	0.49
(11H)	−2.8701	2.326	2.217	1.504	113.28	Buckled	1.0	Spin up: 1.75, spin dn: 0.77
(12H)	−2.9507	2.327	2.161	1.508	114.81	Buckled	0	1.84
(13H)	−2.9019	2.328	2.289	1.513	112.20	Buckled	1.0	Spin up: 2.42, spin dn: 0.99
(14H)	−2.9553	2.346	2.299	1.503	115.84	Buckled	0	2.23

enough to increase the sp^3 portion in the Si–Si covalent bonding. This leads to enhanced buckling in (10H), (11H), (12H), (13H), and (14H) configurations. Consequently, the in-plane angles in these nanoribbons decrease to 112.20°–115.84°.

The structural changes and the presence of H-s orbitals cause electronic variations. As shown in Table 1, the 7ASiNRs can be classified into three groups including semiconductors, metals and spin-splitting materials. The configurations with even number of H atoms absorbed have zero magnetic moment, while those with an odd number of H atoms have magnetic moments of 1 μ_B. Moreover, the $(2H)_{1-14}$, $(2H)_{4-11}$ and $(7H)_{single}$ are exceptional nanoribbons with magnetic moments of 0.74, 0.91 and 7 μ_B, respectively. To discover the mechanism leading to these changes, the electronic structures of 7ASiNRs are calculated and presented in the following sections.

In the previous section, it was shown that H locally perturbs the electronic structure, where sp^3 hybridization becomes stronger due to the contribution of the s orbital from the H adatom. This leaves behind an unpaired π electron on the opposite sublattice, leading to a local magnetic moment of approximately 1 μ_B. However, this value varies depending on H distribution, as shown for the cases of 2 and 7H atom adsorption. The $(2H)_{1-6}$ configuration has one H bonded to first Si atom and the other bonded to the sixth Si atom. Because the two H atoms are close to each other, their magnetic moments couple antiferromagnetically and cancel out. In $(2H)_{1-14}$ and $(2H)_{4-11}$ configurations, the two H atoms are far from each other, weakening the cancellation effect. Therefore, the magnetic moments of $(2H)_{1-14}$ and $(2H)_{4-11}$ configurations are reduced to 0.74 μ_B and 0.91 μ_B, respectively. Meanwhile, the $(7H)_{single}$ configuration has all H atoms adsorbed on only one side, resulting in a magnetic moment of 7 μ_B.

The magnetic moments of the (4H), (6H), (8H), (10H), (12H), and (14H) configurations are zero; therefore, their band structures are presented in Fig. 2 without spin-splitting components. As shown in Fig. 2(a), the pristine 7ASiNR has a direct bandgap, with both the valence band maximum (VBM) and conduction band minimum (CBM) located at the Γ-point. Unlike free-standing silicene, which is gapless,[55] ASiNRs have width-dependent bandgaps as a result of quantum confinement.[56] For the pristine 7ASiNR, the bandgap is 0.65 eV, and the states near the bandgap are primarily constructed from Si-$3p_z$ orbitals. Meanwhile, the Si-$3p_{xy}$ and Si-3s orbitals occupy lower energy levels in the valence bands. Consequently, the Si-$3p_z$ orbitals are responsible for the formation of π bonds, while Si-$3p_{xy}$ and Si-3s orbitals form the σ bonds. However, the overlap of π and σ

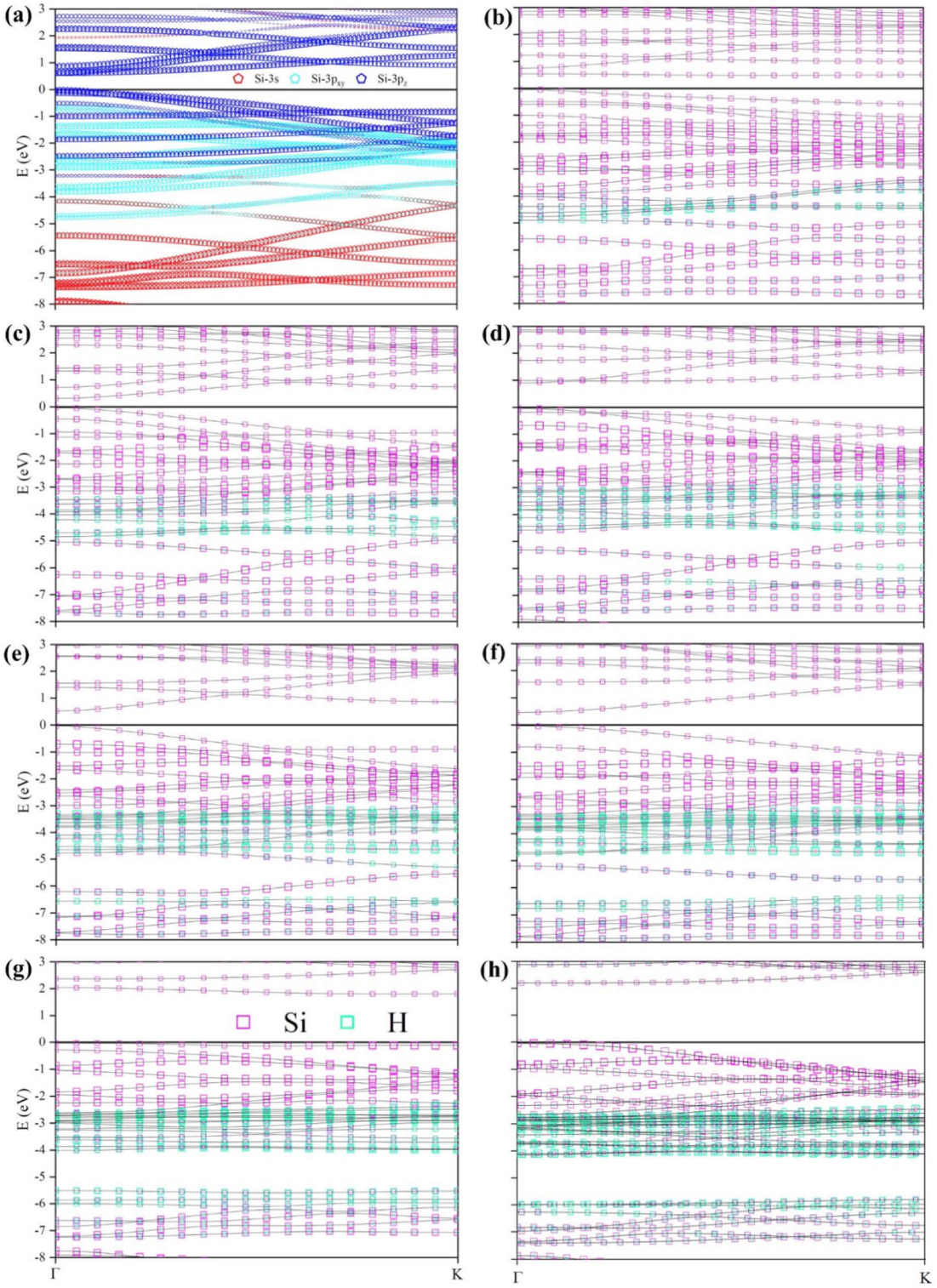

Fig. 2 Orbital- and atom-decomposed electronic band structures of (a) pristine 7ASiNR; (b) $(2H)_{1-6}$, (c) (4H), (d) (6H), (e) (8H), (f) (10H), (g) (12H), and (h) (14H) configurations. The red, cyan, and blue pentagons show the Si-3s, Si-3p_{xy}, and Si-3p_z orbitals, respectively. The magenta and green squares demonstrate the domination of Si and H atoms, respectively.

bands is also observed at the lower valence bands, below −4 eV, indicating the mixing of sp^2 and sp^3 orbitals in the 7ASiNR.

The 7ASiNR passivated by H has a bandgap on the order of 0.5 eV.[27] Substitutional doping modulates this gap only slightly. For example, density-functional studies find that p-type dopants Al, Ga, In, and Tl produce bandgaps of about 0.50–0.51 eV in a 7ASiNR, which is slightly smaller than that of the pristine one.[27] Meanwhile, n-type dopants P, As, Sb, and Bi yield slightly

larger bandgaps (0.52–0.53 eV). At the same time, doping position also plays an important role in determining the bandgap values. Substitution of B or N at the edge of 7ASiNR tends to reduce the bandgap, while co-doping with both B and N can restore a smaller finite bandgap.[57] It is evident that the position and concentration of doping play a key role in establishing the bandgap of ASiNRs. In the case of H-adsorption on 7ASiNRs, all possible adsorption configurations were considered to provide general mechanism governing the bandgap of these nanoribbons. The bandgaps of $(2H)_{1-6}$, (4H), (6H), (8H), (10H), (12H), and (14H) configurations are presented in Table 1, while their band structures are depicted in Fig. 2(b)–(h).

Hybridization between orbitals from H and Si mainly occurs at the lower energy levels of the valence bands from −5 eV to −2.5 eV. At low hydrogen concentrations, only a few Si atoms form bonds with H, which locally disrupts the π-bonding network and generates impurity-like states near the Fermi level. These defect-induced states reduce the effective separation between the VBM and CBM, thereby narrowing the bandgap. As a result, the bandgaps of the $(2H)_{1-6}$, (4H), (8H), and (10H) configurations decrease the bandgaps in the range of 0.33–0.55 eV, compared with 0.65 eV of the pristine 7ASiNR. At high H concentrations, the effect is the opposite: the dense Si–H bonds fully saturate the dangling $3p_z$ orbitals across the ribbons. This saturation forces the Si atoms to rehybridize their orbitals from an sp^2-like state towards a more sp^3-like configuration (similar to bulk silicon). This sp^3 rehybridization removes the π and π* states, which typically form the VBM and CBM near the Fermi level. Therefore, the bandgaps of the (12H) and (14H) configurations are significantly widened to 1.84–2.23 eV. The distribution of H adatoms is also a decisive factor because the bandgap of the (6H) configuration is unexpectedly large, which is 0.92 eV. Meanwhile, the $(2H)_{1-14}$ configuration, having the same 2H atoms adsorbed like the $(2H)_{1-6}$ configuration, exhibits a zero bandgap. Since the H atoms are placed symmetrically at opposite ends of the ribbon, they introduce two electronic states that are strongly localized at the ribbon termini. In nanoribbons like the 7ASiNRs, the end states often reside close to the Fermi level. Because the 7ASiNR has an odd number of sublattices across its width, these localized edge states can couple to form degenerate, flat bands that pin the Fermi level, which is referred to as a zero-energy mode.

As presented in Table 1, the $(2H)_{1-14}$ configuration and other 7ASiNRs adsorbed with an odd number of H atoms have recognizable magnetic moments. Therefore, the spin-splitting band structures of these nanoribbons are plotted in Fig. 3 to characterize their electronic properties. It is obvious that the magnetism of these nanoribbons arises from the clear separation of the spin-up (solid magenta) and spin-down (solid cyan) bands near the Fermi level. Except for the $(2H)_{1-14}$ configuration, the VBM and CBM of other nanoribbons are formed solely by spin-up and spin-down bands, respectively. Therefore, the 7ASiNRs adsorbed with odd number of H atoms can be classified as ferromagnetic semiconductors. As presented in Table 1, these semiconductors have different spin-up and spin-down bandgaps. It is interesting that the magnitudes of these bandgaps are directly proportional to the number of H atoms adsorbed. The spin-up bandgap

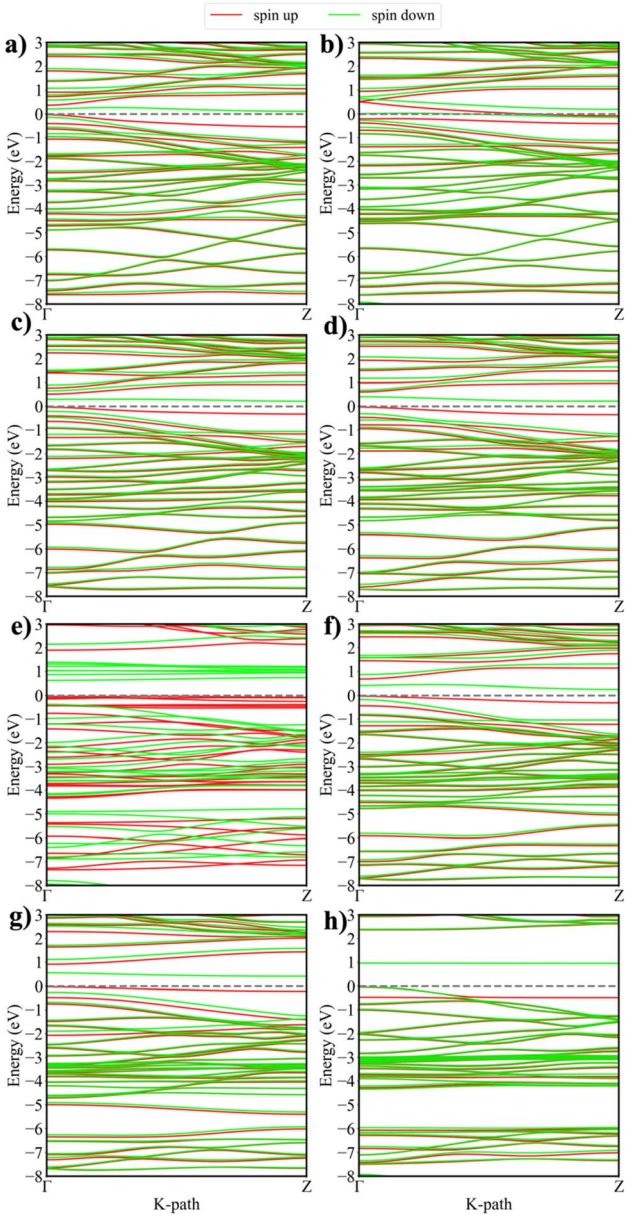

Fig. 3 Spin-splitting electronic band structures of (a) $(1H)_{edge}$, (b) $(2H)_{1-14}$, (c) (3H), (d) (5H), (e) $(7H)_{single}$, (f) (7H), (g) (9H), and (h) (13H) configurations. The solid red and green lines display the spin-up and spin-down bands, respectively. The dashed black line at 0 eV illustrates the Fermi level.

increases from 0.40 eV to 2.42 eV, while the spin-down bandgap ranges from 0.25 eV to 0.99 eV.

The effect of H adsorption on the magnitudes of spin-splitting bandgaps originates from the interaction of H-1s orbitals with the Si-sp^2/sp^3 orbitals. In the pristine 7ASiNR, these π orbitals (arising from Si-$3p_z$ orbitals) extend across the width of the ribbon and form delocalized states near the Fermi level. When a hydrogen atom bonds to a Si atom in the buckled honeycomb lattice it converts that silicon site from sp^2-like bonding toward an sp^3-like local environment and saturates or removes the π (p_z) orbitals from the conduction channel.[58,59] Consequently, the delocalized states are reduced, which widens the bandgap. As

shown in Fig. 2(a), the Si-3p$_z$ orbitals dominate the top of the valence band in pristine 7ASiNRs, spanning from approximately −2.5 eV up to the Fermi level. Therefore, the hybridization of H-1s and Si-3p$_z$ that affects the bandgap of the 7ASiNRs is expected to happen in this energy range. In Fig. 3, this hybridization is characterized by the areas closest to the Fermi level, whereas the spin-up and spin-down bands are clearly separated. For more details, Fig. 3(a) shows the H-1s and Si-3p$_z$ orbital hybridization starting from lower −2.5 eV to 0 eV in the valence band of $(1H)_{edge}$ configuration. In the (3H), (5H), $(7H)_{single\text{-}edge}$, (7H), (9H), and (13H) configurations, as shown in Fig. 3(c)–(h), these orbital hybridization regions are shifted to higher energy levels, signifying that more π-orbitals are saturated. Therefore, the bandgaps of the 7ASiNRs adsorbed with odd number of H atoms becomes wider with the larger number of H atoms.

Adsorption of H atoms at each end of the 7ASiNR results in metallic $(2H)_{1-14}$ configuration. As shown in Fig. 3(b), both the spin-up and spin-down bands cross the Fermi level. It is worth noting that the $(2H)_{1-6}$ configuration has a bandgap of 0.51 eV, as shown in Table 1. These results highlight the significant difference between H adsorptions at the edge and non-edge positions. While the reduction in the bandgap of the $(2H)_{1-6}$ configuration compared to the pristine 7ASiNR was discussed in the previous section. The transformation into gapless $(2H)_{1-14}$ configuration arises from a different mechanism. Silicene nanoribbons have edges with highly reactive dangling bonds. The electronic states associated with the unpassivated edges lie near the Fermi level (E_F) and can reduce the bandgap. Hydrogen passivation removes these states and typically opens up a larger, well-defined bandgap in the semiconducting ASiNR.[60,61] However, adding one more H atom at each edge results in two Si atoms at the edges being over-passivated compared to others. This imbalance breaks the quantum confinement condition and reintroduces states at the Fermi level, ultimately making the nanoribbon metallic.

In pristine 7ASiNR, this system is non-magnetic because the Si-3p$_z$ orbitals are symmetrically distributed and balanced between the two sublattices. When an odd number of hydrogen atoms is adsorbed, this balance is disrupted: some Si atoms retain unsaturated p$_z$ orbitals, while others are converted into sp^3-hybridized states. The unsaturated Si atoms have unpaired p$_z$ electrons, which generate local magnetic moments at the adsorption sites. These local moments give rise to exchange interactions, lifting the spin degeneracy where spin-up and spin-down bands experience different potentials. Consequently, the band structure splits, as shown in Fig. 3, producing distinct bandgaps or even gapless states between the two spin channels. In the case of the $(2H)_{1-14}$ configuration, adsorbing two H atoms at each end does not restore balance to the p$_z$ network. Instead, it oversaturates some edge Si sites, eliminates their π contribution, and breaks the sublattice symmetry. This imbalance leaves unpaired states, leading to a net magnetic moment of 0.74 μ_B (Table 1) and spin polarization, as illustrated in Fig. 3(b). Similarly, adsorption of seven H atoms on only one side of the 7ASiNR produces seven unpaired p$_z$ electrons, with strong spin polarization clearly visible in Fig. 3(e). As a result, the $(7H)_{single\text{-}side}$ configuration exhibits a large magnetic moment of 7 μ_B.

As discussed in the previous section, orbital hybridization between H and Si atoms plays a crucial role in determining the structural and electronic properties of the 7ASiNRs. To gain deeper insight into these effects, it is useful to visualize the energy ranges and intensities of such orbital hybridizations through orbital-projected density of states (DOS) calculations. Fig. 4(a) shows the orbital-projected DOS of the pristine 7ASiNR, with the Fermi level shifted to 0 eV and indicated by the vertical dashed black line. The cyan, green, and blue lines represent the Si-3s, Si-3p$_{xy}$, and Si-3p$_z$ orbitals, respectively. The valence band maximum and conduction band minimum are clearly dominated by Si-3p$_z$ orbitals, corresponding to π-states, and define a direct bandgap of 0.65 eV (Table 1 and Fig. 2(a)). The Si-3p$_{xy}$ orbitals, associated with σ-states, extend over a wide energy range below −0.4 eV, overlapping with both Si-3s and Si-3p$_z$ orbitals. This reflects the sp^2 bonding character, where Si-3s and Si-3p$_{xy}$ orbitals hybridize to form the hexagonal honeycomb lattice observed from the top view. In addition, the partial overlap of Si-3p$_z$ and Si-3p$_{xy}$ orbitals between −3.3 and −0.4 eV introduces a small degree of sp^2/sp^3 mixing, which explains the slight buckling visible in the side view of the 7ASiNR.

Upon adsorption of H atoms, additional H-1s orbitals are introduced into the electronic structure, enhancing the sp^2/sp^3 mixing and locally increasing the sp^3 character around adsorption sites. In Fig. 4(b)–(h), the H-1s orbitals are shown as magenta lines. In the DOSs of the $(2H)_{1-6}$ configuration, depicted in Fig. 4(b), the H-1s orbitals span the entire energy range with varying intensity across different levels. At the VBM, the intensity and distribution of the Si-3p$_z$ orbital changes significantly, while the CBM now consists mainly of Si-3p$_z$, Si-3p$_{xy}$, and H-1s orbitals. This indicates disruption of the π-bonding network and the emergence of impurity-like states near the Fermi level, which explains the reduction of bandgap of the $(2H)_{1-6}$ configuration compared to the pristine 7ASiNR. In the energy range −5 to −2.5 eV, strong hybridization among H-1s, Si-3p$_{xy}$, and Si-3p$_z$ orbitals further enhances the local sp^3 character. As a result, beyond the uniform buckling inherent to sp^2/sp^3 mixing, the $(2H)_{1-6}$ configuration is expected to exhibit stronger local buckling at the hydrogen adsorption sites.

As the number of adsorbed H atoms increases, the aforementioned effects become increasingly pronounced. Fig. 4(c)–(e) show more evident variations in the Si-3p$_z$ states near the VBM and CBM, leading to progressive changes in the bandgaps of the (4H), (6H), and (8H) configurations. Moreover, the sp^2-to-sp^3 transformation associated with hybridization among Si-3p$_z$, Si-3p$_{xy}$, and H-1s orbitals extends deeper into the low-energy region, from approximately −8 to −5 eV. In particular, for the (10H), (12H), and (14H) configurations, Fig. 4(f)–(h) reveal the emergence of new peaks below −6 eV in the valence band. This enhanced hybridization not only reshapes the DOS but also correlates with a significant increase in the bandgap observed in these highly hydrogenated systems.

The magnetic properties of 7ASiNRs with an odd number of adsorbed H atoms, including $(1H)_{edge}$, (3H), (5H), $(7H)_{double\text{-}side}$, (9H), and (13H) along with the special cases of $(2H)_{1-14}$ and

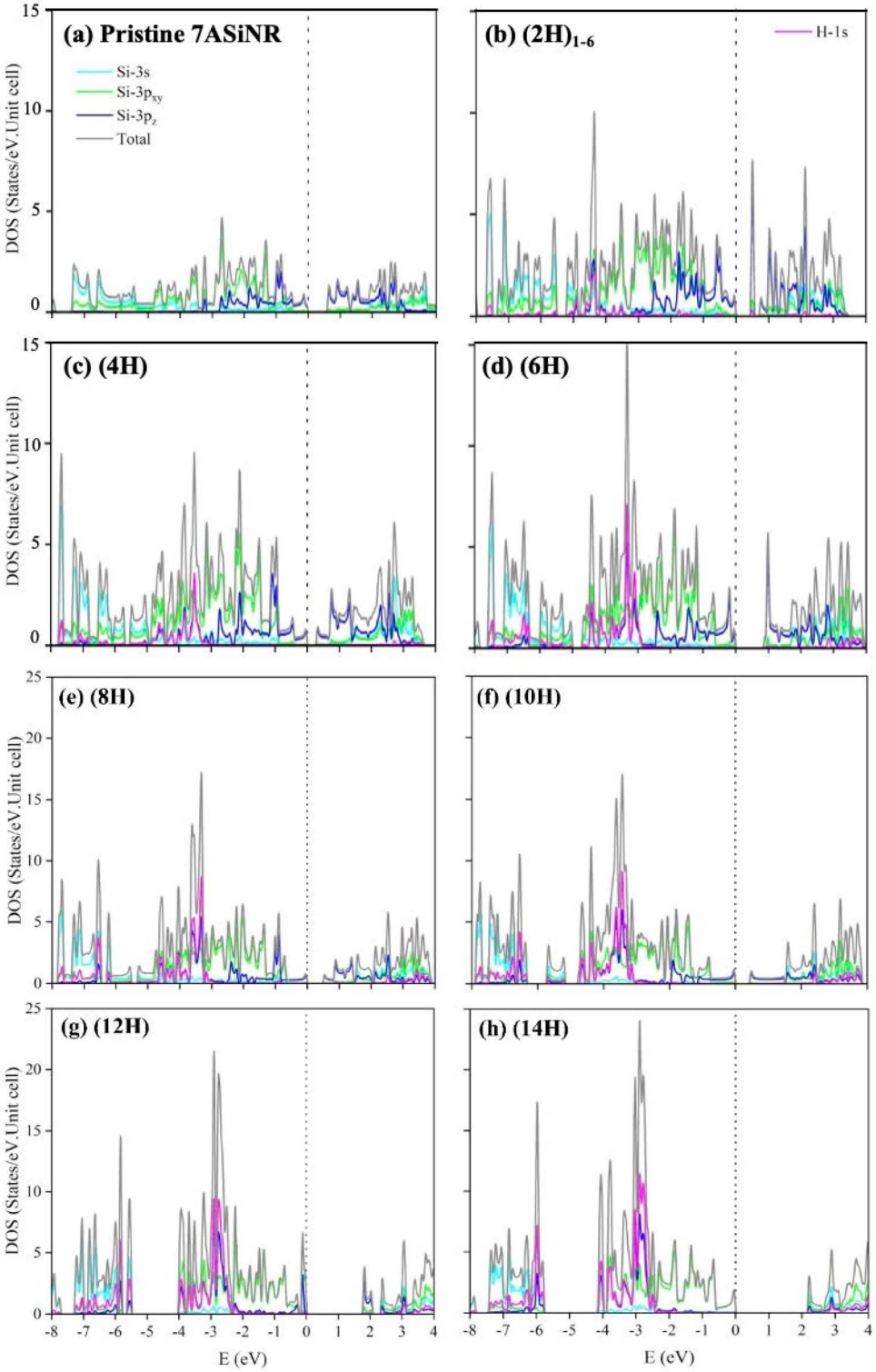

Fig. 4 Orbital-projected density of states (DOSs) of (a) pristine 7ASiNR, (b) $(2H)_{1-6}$, (c) (4H), (d) (6H), (e) (8H), (f) (10H), (g) (12H), and (h) (14H) configurations. The solid cyan, green, blue, and magenta curves display for the Si-3s, Si-3p_{xy}, Si-3p_z, and H-1s orbitals, respectively.

$(7H)_{single\text{-}side}$, can be further examined through their orbital- and spin-projected DOS. In Fig. 5, the total DOS is depicted in black, while the contributions from Si-3s, Si-3p_{xy}, Si-3p_z, and H-1s orbitals are represented in cyan, green, blue, and magenta, respectively.

In the DOS of the $(1H)_{edge}$ configuration, shown in Fig. 5(a), the H-1s orbitals contribute across the entire energy spectrum from the valence to the conduction bands with varying intensities and strong spin polarization. The Si-3p_z orbitals, which dominate both the VBM and CBM, become highly polarized

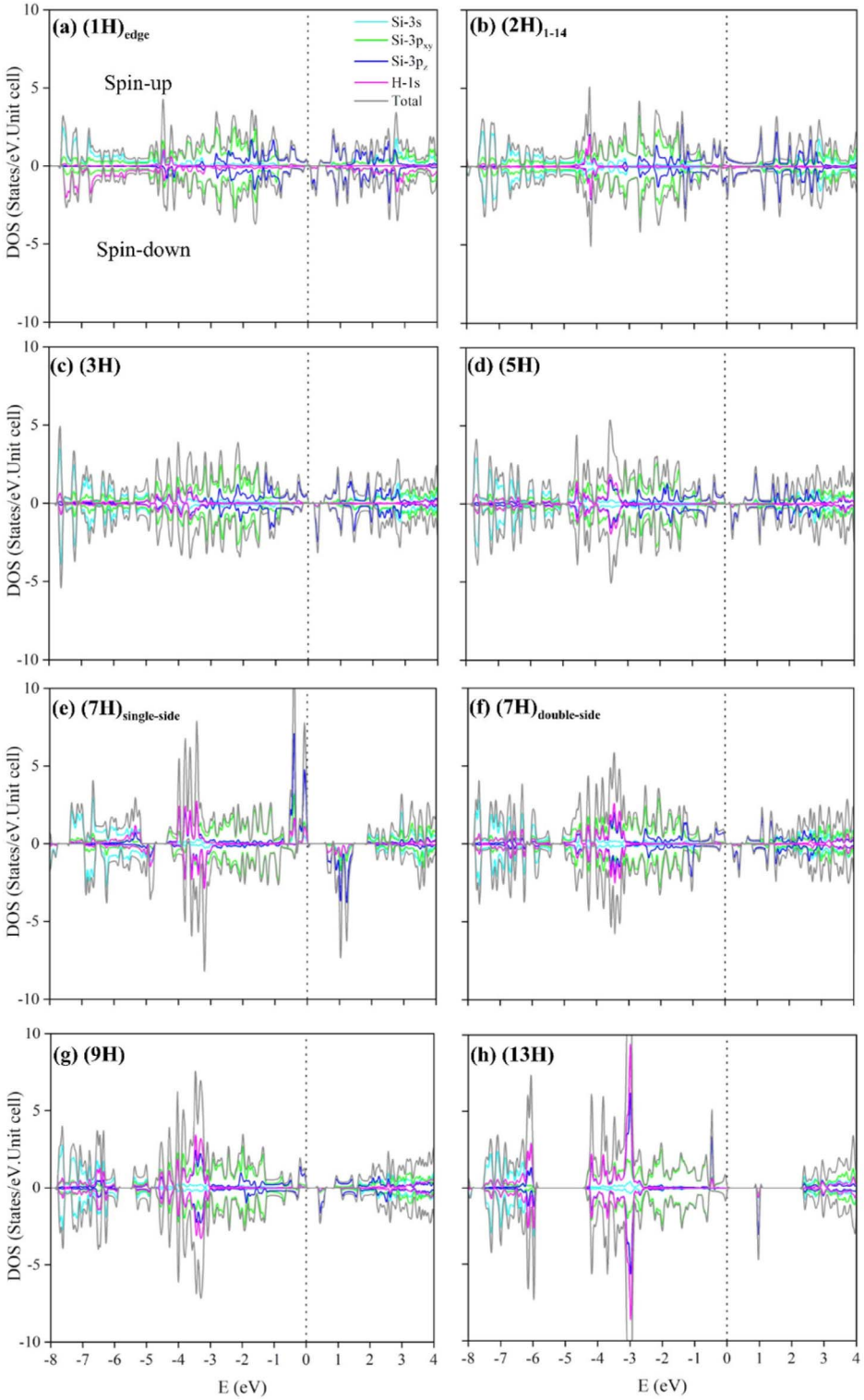

Fig. 5 Orbital- and spin-projected density of states (DOSs) of (a) $(1H)_{edge}$, (b) $(2H)_{1-14}$, (c) (3H), (d) (5H), (e) $(7H)_{single\text{-}side}$, (f) $(7H)_{double\text{-}side}$, (g) (9H), and (h) (13H) configurations. The solid cyan, green, blue, and magenta curves display the Si-3s, Si-$3p_{xy}$, Si-$3p_z$, and H-1s orbitals, respectively.

near the Fermi level through hybridization with the H-1s orbitals. This spin asymmetry, particularly pronounced in the range from −1 to 0 eV, generates a net magnetic moment of 1 μ_B, thereby transforming the $(1H)_{edge}$ configuration into a ferromagnetic semiconductor. The mismatch between spin-up and spin-down DOS also results in different bandgaps for the two spin channels: 0.40 eV for spin-up and 0.25 eV for spin-down states. Meanwhile, the Si-$3p_{xy}$ and Si-3s orbitals are

mainly distributed at energies below −1 eV in the valence band and above 0.7 eV in the conduction band. In the range −4.5 to −4 eV, significant hybridization occurs among H-1s, Si-3p_{xy}, and Si-3p_z orbitals, introducing additional sp^3 character. This localized sp^2/sp^3 mixing enhances structural buckling at the hydrogen adsorption site in the $(1H)_{edge}$ configuration.

In the $(2H)_{1-14}$ configuration, shown in Fig. 5(b), the spin asymmetry near the Fermi level is relatively weak. As a result, this configuration exhibits only a small net magnetic moment of 0.74 μ_B, as presented in Table 1. In contrast, the (3H), (5H), $(7H)_{double\text{-}side}$, (9H), and (13H) configurations, shown in Fig. 5(c), (d), (f)–(h), exhibit more pronounced spin asymmetry near the Fermi level, resulting in a magnetic moment of 1 μ_B. This moment remains unchanged with additional hydrogen adsorption because, in every case, the two unpaired Si-3p_z electrons on opposite sides cancel one another, leaving only one free unpaired Si-3p_z electron. The structural modification, on the other hand, becomes more pronounced with increasing hydrogenation because the contribution of sp^3 character also grows due to stronger hybridization among H-1s, Si-3p_{xy}, and Si-3p_z orbitals. Fig. 5(c)–(h) clearly illustrate the progressive increase in both intensity and energy range of this hybridization within the valence band. This enhanced mixing reflects a gradual transformation from sp^2-dominated bonding toward sp^3-rich bonding environments. Consequently, the 7ASiNRs with higher hydrogen coverage develop more uniformly buckled structures, as stronger sp^2/sp^3 mixing drives larger local lattice distortions. A representative example is the fully hydrogenated (14H) configuration shown in Fig. 1(d), which exhibits a highly uniform buckled geometry.

To increase the number of free unpaired Si-3p_z electrons, seven H atoms are adsorbed on one side of the 7ASiNR. As shown in Fig. 5(e), the DOS of the $(7H)_{single\text{-}side}$ configuration exhibits a pronounced asymmetric spin distribution. In the energy range from −1.0 to −0.6 eV, spin-down states dominate, whereas in the interval from −0.6 to 0 eV, the spin-up states show much higher intensities than their spin-down counterparts. This strong spin splitting near the Fermi level gives rise to a large magnetic moment, consistent with the presence of seven unpaired Si-3p_z electrons localized along one edge. A smaller degree of spin splitting is also evident at deeper valence-band energies, reinforcing the overall spin polarization of the system. These features are well captured in the spin-splitting band structure of the $(7H)_{single\text{-}side}$ configuration shown in Fig. 3, whereas the spin-up and spin-down bands are clearly separated. In addition, sp^3 hybridization among H-1s, Si-3p_{xy}, and Si-3p_z orbitals appears in the energy range from −4.5 eV to −3.2 eV, indicating enhanced mixing at low-lying states. Notably, such hybridization is observed near the valence-conduction band edges, where it strongly modifies the bandgap by disrupting the π-bonding network and introducing impurity-like states.

The magnetic properties of 7ASiNRs following adsorption of an odd number of H atoms were quantified in previous sections, with the resulting magnetic moments for each ferromagnetic nanoribbon presented in Table 1. To understand the origins of this magnetism, we first examined the spin-splitting band structures (Fig. 3). More detailed insight is provided by the orbital- and spin-projected density of states (Fig. 5), which highlight the critical role of hybridization between H and Si orbitals. This section further explores these findings by presenting the spin density distributions (Fig. 6). These visualizations clearly reveal the spatial distribution of spin and illustrate how H adsorption gives rise to the observed differences in magnetic moments.

Fig. 6(a) and (b) present the spin density distributions of the $(1H)_{edge}$ and $(1H)_{non\text{-}edge}$ configurations in both top and side views, whereas the spin-up and spin-down densities are represented by yellow and cyan regions, respectively. In these configurations, the adsorption of a single H atom enhances the spin-up density at the adsorption site and its three neighboring Si atoms, while the remainder of the nanoribbon exhibits a uniform distribution of spin-up and spin-down states. This asymmetry in spatial spin distribution induces the magnetic moments of the $(1H)_{edge}$ and $(1H)_{non\text{-}edge}$ configurations. For the $(2H)_{1-14}$ and $(2H)_{4-11}$ configurations, whereas two H atoms are adsorbed at the positions far apart, the spin imbalance across the inversion center is reduced, leading to a lower magnetic moment. As the number of adsorbed H atoms increases to from 3H to 13H, shown in Fig. 6(e)–(j), the spin polarizations associated with each pair of H atoms cancel, leaving only the contribution from the final unpaired H atom. At this site, the spin-up density accumulates, resulting in magnetic moments of 1 μ_B for the (3H), (5H), $(7H)_{double\text{-}side}$, (9H), and (13H) configurations identical to those of the $(1H)_{edge}$ and $(1H)_{non\text{-}edge}$ cases. The spin density distribution of $(7H)_{single\text{-}side}$ configuration, as depicted in Fig. 6(g), is an exceptional case. Herein, adsorption of seven H atoms on one side prevents cancellation of the Si-3p_z electrons, producing strong spin polarization. Consequently, the $(7H)_{single}$ configuration exhibits strong ferromagnetism with a magnetic moment of 7 μ_B.

It is well known that the interaction between adsorbed atoms and neighboring host atom orbitals causes charge redistribution, leading to regions of charge accumulation and depletion.[13,16] Such variations in the local charge environment directly influence the bonding characteristics and electronic structure of the nanoribbons. To further clarify the role of hydrogen adsorption in 7ASiNRs, the charge density distribution and charge density difference were calculated for pristine 7ASiNR, as well as for the $(1H)_{edge}$, (7H), and (14H) configurations. The charge density, expressed in elementary charge per unit cell volume (ea_0^{-3}), is visualized with red regions denoting the highest electron density and blue regions indicating the lowest. For pristine 7ASiNR, the charge density distribution, shown in Fig. 7(a), clearly reflects the Si–Si covalent bonding. The space connecting adjacent Si atoms is filled with orange regions, signifying strong electron accumulation in the σ-bonds formed through hybridization of the Si-3s and Si-3p_{xy} orbitals. In contrast, the green regions around the Si–Si bonds correspond to lower electron density in the π-bonds, which arise from the unsaturated Si-3p_z orbitals. These features are consistent with the orbital-projected density of states of pristine 7ASiNR, presented in Fig. 4(a).

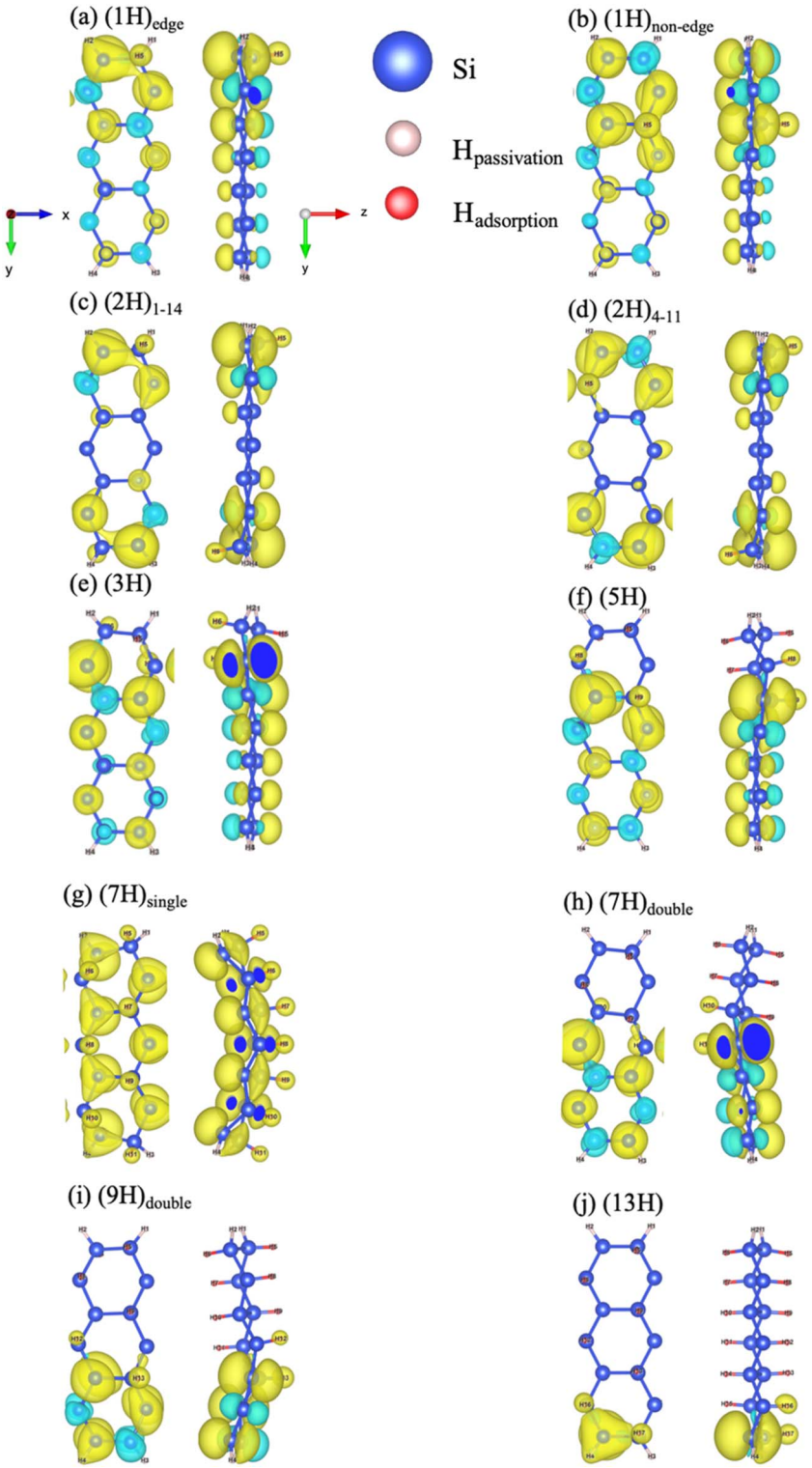

Fig. 6 Spatial spin density distribution of (a) $(1H)_{edge}$, (b) $(1H)_{non\text{-}edge}$, (c) $(2H)_{1-14}$, (d) $(2H)_{4-11}$, (e) (3H), (f) (5H), (g) $(7H)_{single\text{-}side}$, (h) $(7H)_{double\text{-}side}$, (i) (9H), and (j) (13H) configurations. The yellow and cyan isosurface show the spin-up and spin-down orientations, respectively.

Upon adsorption of a single H atom, a significant amount of charge is transferred to the adsorption site, as indicated by the red region surrounding the H atom in Fig. 6(b) for the $(1H)_{edge}$ configuration. The corresponding charge density difference, shown in Fig. 6(c), further reveals charge accumulation in a spherical region oriented perpendicular to the nanoribbon. This charge transfer originates from the formation of a saturated π-bond, through hybridization between H-1s and Si-$3p_z$

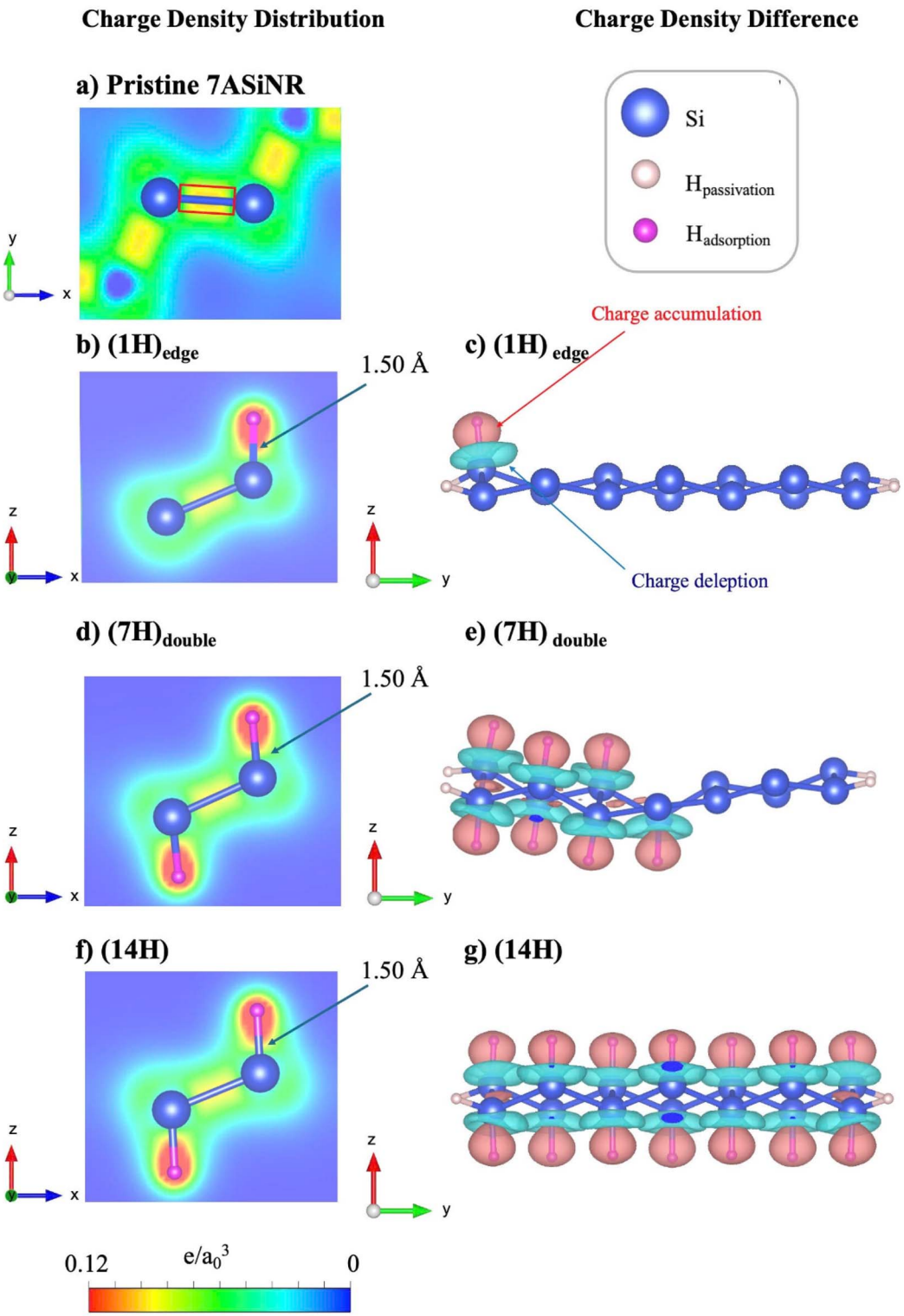

Fig. 7 Charge density distribution of (a) pristine 7ASiNR, (b) $(1H)_{edge}$, (d) (7H), and (f) (14H) configurations; Charge density difference of (c) $(1H)_{edge}$, (e) (7H), and (g) (14H) configurations.

orbitals. In addition, hybridization between H-1s and Si-3p_{xy} orbitals forms in-plane σ-bonds with comparatively lower electron density, as evidenced by the reduced orange color in the region between adjacent Si atoms. The blue regions in Fig. 6(c), corresponding to charge depletion, reflect the redistribution of electrons from σ-bonds into π-bonds. With increasing numbers of adsorbed H atoms, as illustrated in Fig. 7(c), (e), and (g), multiple centers of charge accumulation and depletion emerge,

which can be regarded as local dipoles. In the (14H) configuration, these dipoles cancel one another due to their opposite orientations, resulting in a non-magnetic semiconducting state. By contrast, in the $(1H)_{edge}$ and $(7H)_{double}$ configurations, a single unpaired dipole remains, giving rise to ferromagnetic semiconducting behavior.

In summary, edge hydrogen adsorption has been shown to plays a decisive role in tailoring the magnetic behavior of silicene nanoribbons through spin–orbit coupling effect.[62,63] In 7ASiNRs, the H edge adsorption induces magnetism by selectively removing or preserving edge Si-$3p_z$ dangling-bond states that drive spin polarization. The magnetic response follows a clear even–odd parity rule: configurations with an odd number of hydrogen atoms (*e.g.*, 1H, 3H, 5H, 7H, 9H, 13H) retain one uncompensated π electron between the two edges, resulting in a robust net moment of 1 μ_B through exchange splitting of the remaining edge state. In contrast, even-H configurations (2H, 4H, 6H, 8H, 10H, 12H, 14H) generally achieve complete passivation of paired edge dangling bonds, suppressing magnetism and producing a non-magnetic ground state. An important exception is the partially symmetric double-edge adsorption case $(2H)_{1-14}$, where both edges are oversaturated but still host weakly localized states near E_F; the resulting incomplete spin compensation yields a reduced moment of 0.74 μ_B and metallic spin polarization. Thus, selective edge hydrogenation, by modulating the balance of edge π orbitals and exchange interactions, acts as an efficient on-demand magnetic switch, enabling transitions between non-magnetic semiconducting, integer-spin ferromagnetic, and weakly spin-polarized metallic states in armchair silicene nanoribbons.

4. Conclusion

In this work, first-principles density functional theory (DFT) calculations were employed to comprehensively study the structural, electronic, and magnetic properties of hydrogenated 7-armchair silicene nanoribbons (7ASiNRs). A wide range of hydrogen adsorption configurations including edge, non-edge, single-side, and double-side sites with 1 to 14 hydrogen atoms were systematically modeled and analyzed. Based on adsorption energy and geometric analysis, 17 stable configurations were identified, demonstrating that hybridization between the H-1s and Si-sp^2/sp^3 orbitals plays a decisive role in determining the stability and atomic arrangement of the 7ASiNRs. Hydrogen adsorption not only strengthens local Si–H and Si–Si bonds but also enhances the sp^3 character, thereby increasing the buckling amplitude of the ribbon. The interplay between H coverage and hybridization leads to a gradual transition from planar, sp^2-dominated to buckled, sp^3-rich structures. The electronic structures of hydrogenated 7ASiNRs reveal three distinct classes: semiconducting, metallic, and spin-polarized systems. Configurations with even numbers of H atoms are nonmagnetic semiconductors, while those with odd numbers of H atoms exhibit ferromagnetism due to unpaired Si-$3p_z$ electrons localized near adsorption sites. Remarkably, the $(7H)_{single}$ configuration shows a strong spin polarization with a total magnetic moment of 7 μ_B, whereas the $(2H)_{1-14}$ configuration transitions into a metallic state owing to over-passivation at the ribbon edges. Bandgap modulation in the 7ASiNRs arises from the balance between two competing effects: (i) disruption of delocalized π-orbitals by low hydrogen coverage, which narrows the bandgap, and (ii) π-orbital saturation and enhanced sp^3 hybridization at high coverage, which widens it. These mechanisms are clearly supported by the orbital-projected and spin-resolved density of states, which show that the strong hybridization between the H-1s and Si-$3p_z$/Si-$3p_{xy}$ orbitals across both valence and conduction bands. Charge and spin density analyses further confirm that hydrogen adsorption induces charge redistribution and local dipole formation, while breaking sublattice symmetry and introducing spin imbalance. The resulting structural buckling, spin splitting, and tunable magnetism underscore the versatile behavior of hydrogenated 7ASiNRs. In summary, this study establishes a comprehensive picture of how hydrogen adsorption modulates the atomic, electronic, and magnetic characteristics of 7-armchair silicene nanoribbons. The insights gained here not only clarify the underlying orbital interactions responsible for these effects but also highlight the strong potential of H-functionalized armchair silicene nanoribbons as controllable materials for next-generation nanoelectronic and spintronic applications.

Author contributions

D. M. Hoat: investigation, data curation, methodology, visualization, formal analysis, writing – original draft. Duong Trong Nhan: investigation, visualization, formal analysis, writing – reviewing and editing. Vuong Minh Duc: investigation, data curation, visualization. Le Phuong Truong: investigation, visualization, formal analysis, writing – reviewing and editing. Tam V.-T. Mai: investigation, visualization, software, formal analysis, writing – reviewing and editing. Minh-Triet Dang: investigation, visualization, software, formal analysis, validation, writing – reviewing and editing. Duy Khanh Nguyen: supervision, conceptualization, investigation, data curation, validation, resources, funding acquisition, formal analysis, writing – reviewing and editing.

Conflicts of interest

The authors declare that they have no known competing financial interests or personal relationships that could have appeared to influence the work reported in this paper.

Data availability

The data that supports the findings of this study are available within the article.

Acknowledgements

Duy Khanh Nguyen gratefully acknowledges the support of Van Lang University (VLU) and extends his warmest congratulations to the university on its 30th anniversary celebration in November 2025.

References

1 K. S. Novoselov, A. K. Geim, S. V. Morozov, D. Jiang, Y. Zhang, S. V. Dubonos, I. V. Grigorieva and A. A. Firsov, *Science*, 2004, **306**, 666–669.
2 P. Vogt, P. De Padova, C. Quaresima, J. Avila, E. Frantzeskakis, M. C. Asensio and G. Le Lay, *Phys. Rev. Lett.*, 2012, **108**, 155501.
3 D. K. Nguyen, N. T. T. Tran, Y. H. Chiu and M. F. Lin, *Sci. Rep.*, 2019, **9**, 1–15.
4 M. E. Dávila, L. Xian, S. Cahangirov, A. Rubio and G. Le Lay, *New J. Phys.*, 2014, **16**, 095002.
5 K. F. Mak, C. Lee, J. Hone, J. Shan and T. F. Heinz, *Phys. Rev. Lett.*, 2010, **105**, 136805.
6 R. Galland, P. Leduc, C. Guérin, D. Peyrade, L. Blanchoin and M. Théry, *Nat. Mater.*, 2013, **12**, 416–421.
7 V. Khuong Dien, P. Thi Bich Thao, N. Thi Han, N. Duy Khanh, L. V. Phuong Thuan, M. F. Lin and N. Thanh Tien, *Phys. Rev. B: Condens. Matter*, 2023, **108**, 205406.
8 V. K. Dien, N. T. Tien, N. D. Khanh, N. T. N. Han and M. F. Lin, *Phys. Rev. B: Condens. Matter*, 2023, **108**, 205150.
9 A. Castellanos-Gomez, L. Vicarelli, E. Prada, J. O. Island, K. L. Narasimha-Acharya, S. I. Blanter, H. S. Van Der Zant, *et al.*, *2D Mater.*, 2014, **1**, 025001.
10 D. K. Nguyen, C. V. Ha, J. Guerrero-Sanchez and D. M. Hoat, *RSC Adv.*, 2025, **15**, 5096–5104.
11 N. H. Dang, P. T. B. Thao, H. T. Hoang, N. C. D. Vinh, K. D. Vo, N. T. Tien and D. K. Nguyen, *J. Magn. Magn. Mater.*, 2024, **607**, 172394.
12 N. T. Tien, N. H. Dang, P. T. Bich Thao, K. D. Vo, D. M. Hoat and D. K. Nguyen, *RSC Adv.*, 2024, **14**, 16445–16458.
13 D. P. Dam, P. T. Bich Thao, T. Pham, M. N. Qui, V. K. Dien, N. T. Tien and D. K. Nguyen, *Ceram. Int.*, 2025, DOI: 10.1016/j.ceramint.2025.07.042.
14 D. M. Hoat, V. Khuong Dien, T. Pham, Q. Duy Ho, H. A. Huy, D. K. Nguyen and V. D. Dat, *Phys. E*, 2025, **172**, 116284.
15 D. M. Hoat, V. K. Dien, Q. D. Ho, D. P. Dam, N. T. Tien and D. K. Nguyen, *Phys. Chem. Chem. Phys.*, 2024, **26**, 15939–15956.
16 D. M. Hoat, K. D. Vo, N. T. T. Tran, Q. D. Ho, M. T. Dang, H. A. Huy, D. T. Nhan and D. K. Nguyen, *RSC Adv.*, 2025, **15**, 27139–27153.
17 D. K. Nguyen, Y. T. Lin, S. Y. Lin, Y. H. Chiu, N. T. T. Tran and M. Fa-Lin, *Phys. Chem. Chem. Phys.*, 2017, **19**, 20667–20676.
18 D. K. Nguyen, N. T. T. Tran, T. T. Nguyen and M. F. Lin, *Sci. Rep.*, 2018, **8**, 1–12.
19 N. T. T. Tran, G. Gumbs, D. K. Nguyen and M. F. Lin, *ACS Omega*, 2020, **5**, 13760–13769.
20 H. D. Pham, S. Y. Lin, G. Gumbs, N. D. Khanh and M. F. Lin, *Front. Phys.*, 2020, **8**, 561350.
21 D. K. Nguyen, D. Q. Hoang and D. M. Hoat, *RSC Adv.*, 2022, **12**, 9828–9835.
22 K. Shakouri, *et al.*, *Phys. Rev. B: Condens. Matter*, 2015, **92**, 035413.
23 M. Ferri, G. Fratesi, G. Onida and A. Debernardi, *Phys. Rev. B: Condens. Matter*, 2019, **99**, 085414.
24 L. Masson and G. Prévot, *Nanoscale Adv.*, 2023, **5**, 1574–1599.
25 B. Aufray, *et al.*, *Appl. Phys. Lett.*, 2010, **96**, 183102.
26 G. Guo, Y. Xu, S. Tan, F. Du and G. Xu, *Phys. Lett. B*, 2023, **37**, 2350056.
27 S. Singh, A. De Sarkar, B. Singh and I. Kaur, *RSC Adv.*, 2017, **7**, 12783–12792.
28 R. Kalami and S. A. Ketabi, *J. Electron. Mater.*, 2023, **52**, 6566–6577.
29 S. M. Aghaei, M. M. Monshi, I. Torres and I. Calizo, *RSC Adv.*, 2016, **6**, 17046–17058.
30 D. Zhang, M. Long, F. Xie, J. Ouyang, H. Xu and Y. Gao, *Sci. Rep.*, 2016, **6**, 1–7.
31 D. Nguyen, V. Dat, Vo Van On and Ming-Fa Lin, *Emerging Mater. Res.*, 2022, 32–41.
32 T. T. Nguyen, V. N. Hoang, T. P. T. Huynh, D. K. Nguyen and V. O. Vo, *Phys. E*, 2022, **142**, 115309.
33 B. M. Wong, S. H. Ye and G. O'Bryan, *Nanoscale*, 2012, **4**, 1321–1327.
34 Y. W. Son, M. L. Cohen and S. G. Louie, *Nature*, 2006, **444**, 347–349.
35 X. Q. Wang, H. D. Li and J. T. Wang, *Phys. Chem. Chem. Phys.*, 2012, **14**, 3031–3036.
36 M. Houssa, E. Scalise, K. Sankaran, G. Pourtois, V. V. Afanas'Ev and A. Stesmans, *Appl. Phys. Lett.*, 2011, **98**, 223107.
37 J. Qiu, H. Fu, Y. Xu, Q. Zhou, S. Meng, H. Li, L. Chen and K. Wu, *ACS Nano*, 2015, **9**, 11192–11199.
38 D. Solonenko, *et al.*, *Phys. Rev. B: Condens. Matter*, 2017, **96**, 235423.
39 Q. D. Ho and E. Rauls, *ChemistrySelect*, 2023, **8**, e202302266.
40 Q. Duy Ho and M. Castillo, *Comput. Mater. Sci.*, 2023, **216**, 111827.
41 Q. D. Ho, K. D. Vo, N. Thanh Tien, H. A. Huy, D. Q. Hoang and D. K. Nguyen, *RSC Adv.*, 2025, **15**, 5889–5894.
42 Q. D. Ho and E. Rauls, *Mater. Today Commun.*, 2023, **36**, 106875.
43 G. Kresse and J. Hafner, *Phys. Rev. B: Condens. Matter*, 1993, **47**, 558–561.
44 G. Kresse and J. Furthmüller, *Comput. Mater. Sci.*, 1996, **6**, 15–50.
45 B. Hammer, L. B. Hansen and J. K. Nørskov, *Phys. Rev. B: Condens. Matter*, 1999, **59**, 7413–7421.
46 P. E. Blöchl, *Phys. Rev. B: Condens. Matter*, 1994, **50**, 17953–17979.
47 H. Behera and G. Mukhopadhyay, *AIP Conf. Proc.*, 2010, **1313**, 152–155.
48 G. Chakraborty, R. Padmashree and A. Prasad, *Mater. Sci. Eng., B*, 2023, **297**, 116817.
49 R. Wang, M. S. Xu and X. D. Pi, *Chin. Phys. B*, 2015, **24**, 086807.
50 S. Cahangirov, M. Topsakal, E. Aktürk, H. Šahin and S. Ciraci, *Phys. Rev. Lett.*, 2009, **102**, 236804.
51 J. Vejpravová, *Nanomaterials*, 2021, **11**, 2469.
52 M. Takahashi, *ACS Omega*, 2021, **6**, 12099–12104.

53 K. Gherbi, M. T. Kadri, H. Belkhir and K. Zanat, *Phys. Open*, 2025, **24**, 100280.
54 I. V. Kosarev, S. V. Dmitriev, A. S. Semenov and E. A. Korznikova, *Materials*, 2022, **15**, 5900.
55 M. Houssa, A. Dimoulas and A. Molle, *J. Phys. Condens. Matter.*, 2015, **27**, 253002.
56 D. Zhang, M. Long, F. Xie, J. Ouyang, H. Xu and Y. Gao, *Sci. Rep.*, 2016, **6**, 23677.
57 F. B. Zheng, C. W. Zhang, S. S. Yan and F. Li, *J. Mater. Chem. C*, 2013, **1**, 2735–2743.
58 A. Podsiadły-Paszkowska and M. Krawiec, *Condens. Matter*, 2017, **2**, 1–10.
59 P. Zhang, X. D. Li, C. H. Hu, S. Q. Wu and Z. Z. Zhu, *Phys. Lett. A*, 2012, **376**, 1230–1233.
60 S. Mehdi Aghaei and I. Calizo, *MRS Adv.*, 2016, **1**, 1613–1618.
61 Q. G. Jiang, J. F. Zhang, Z. M. Ao and Y. P. Wu, *J. Mater. Chem. C*, 2015, **3**, 3954–3959.
62 Y. Han, L. Wu, Z. Wang and S. Wang, *Phys. B: Condens. Matter.*, 2023, **649**, 414445.
63 X. F. Yang, Y. S. Liu, J. F. Feng, X. F. Wang, C. W. Zhang and F. Chi, *J. Appl. Phys.*, 2014, **116**, 124312.